Unusual Angular Dependence of the Raman Response in Black Phosphorus

Henrique B. Ribeiro,[†] Marcos A. Pimenta,[‡] Christiano J. S. de Matos,[*,†] Roberto Luiz Moreira,[‡] Aleksandr S. Rodin,[§] Juan D. Zapata,[†,⊥] Eunézio A. T. de Souza,[†] and Antonio H. Castro Neto[§,∥,¶]

[†]Mackgraphe-Graphene and Nanomaterials Research Center, Mackenzie Presbyterian University, 01302-907 São Paulo, Brazil, [‡]Departamento de Física, UFMG, 30123-970 Belo Horizonte, Brazil, [§]Centre for Advanced 2D Materials and Graphene Research Centre Faculty of Science, National University of Singapore, 119077 Singapore, [⊥]Universidad de Antioquia, Medellin Colombia, [∥]Department of Physics Faculty of Science, National University of Singapore, 119077 Singapore, and [¶]National Graduate School for Integrative Sciences & Engineering, National University of Singapore, 119077 Singapore

ABSTRACT Anisotropic materials are characterized by a unique optical response, which is highly polarization-dependent. Of particular interest are layered materials formed by the stacking of two-dimensional (2D) crystals that are naturally anisotropic in the direction perpendicular to the 2D planes. Black phosphorus (BP) is a stack of 2D phosphorene crystals and a highly anisotropic semiconductor with a direct band gap. We show that the angular dependence of polarized Raman spectra of BP is rather unusual and can be explained only by considering complex values for the Raman tensor elements. This result can be traced back to the electron–photon and electron–phonon interactions in this material.

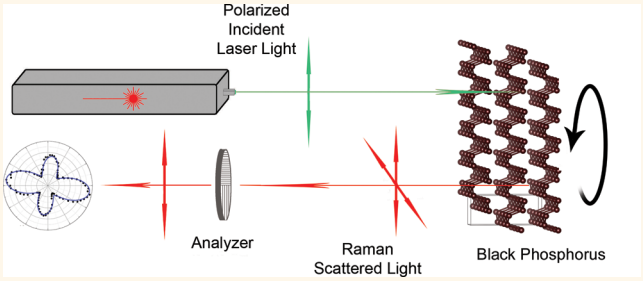

KEYWORDS: black phosphorus · phosphorene · polarized Raman spectroscopy · linear dichroism · electron–phonon coupling

Black phosphorus (BP) is a thermodynamically stable allotrope of phosphorus that, similarly to graphite and transition metal dichalcogenides, exhibits a layered structure from which 2D crystals can be obtained by mechanical exfoliation.[1−7] In this work, we study the Raman spectra and the angular dependence of the Raman spectra in BP by analyzing the scattered light at polarizations both parallel and perpendicular to the incident polarization and using three different laser lines (488, 532, and 633 nm). We show that, while the angular dependence of the B_{2g} Raman mode is well-explained considering real values for the Raman tensor elements, the totally symmetric Raman modes with A_g symmetry exhibit an anomalous angular dependence, which only could be described by assuming complex values for the Raman tensor elements.[8] From the analysis of the angular dependence results, we obtained the phase difference between the Raman tensor elements of the totally symmetric modes. It was observed that the relative phase for the in-plane A_g^2 is much larger than that of the out-of-plane A_g^1. The laser energy dependence of the absolute values and phase differences of the Raman tensor elements are presented, and our results are discussed in terms of the anisotropy and of the linear dichroism of BP.

Since the Raman response is directly related to the electron–phonon coupling, our results put strigent constraints on the way electrons and ions interact in BP. This is of particular interest given that under pressure BP changes from a direct band gap semiconductor to an indirect band gap semicondutor and eventually to a metal.[9] In the metallic phase, BP undergoes a superconducting transition with critical temperatures up to 11 K, which is still unexplained but could be the result of the electron–phonon coupling.[10,11]

The bulk structure of BP has an orthorhombic symmetry belonging to the point (space) group D_{2h}^{18} (*Cmca*),[12] with four atoms per unit cell (see Figure S1 in Supporting Information). BP has a puckered layered structure, with strong anisotropy in the basal plane, which is reflected by its physical properties.[2,5] Unlike other layered materials, BP is a direct band gap semiconductor[13] in both bulk and single- and few-layer forms, and the band gap energy

* Address correspondence to cjsdematos@mackenzie.br.

Received for review January 30, 2015 and accepted March 9, 2015.

Published online March 09, 2015
10.1021/acsnano.5b00698

increases with a decreasing number of layers. This characteristic may lead to important optoelectronic and photonic applications, and electronic and optical properties of bulk BP are well reported in the literature.[13−16]

Raman spectroscopy was extensively used in the past to study the phonon structure and lattice dynamics of BP, and the assignment of the Raman modes is well-established.[17−23] More recently, Raman spectroscopy became a very useful tool for the study and characterization of two-dimensional BP.[3,7,24] The effect of the incident light polarization on the BP Raman spectra was reported recently,[19,25] but polarized Raman spectroscopy, with a complete angular dependence characterization, which includes resolving the polarization of scattered radiation, was still missing in the literature. From the fitting of the angular dependence of the polarized spectra, we could measure the absolute values and relative phases of the Raman tensor elements, and this result is associated with the linear dichroism in BP. Our results provide a deeper understanding of the interaction between BP and light, and therefore, they are helpful in advancing the possible use of this material in photonics and optoelectronics. We note that, during the final preparation stage of this article, another report on angle-resolved polarized Raman spectroscopy of BP became available.[26] While most of the experimental results reported therein agree with those presented here, no attempt is made to quantitatively match the data to theory, and therefore, no mention is made of the need to take into account BP's dichroism during this task.

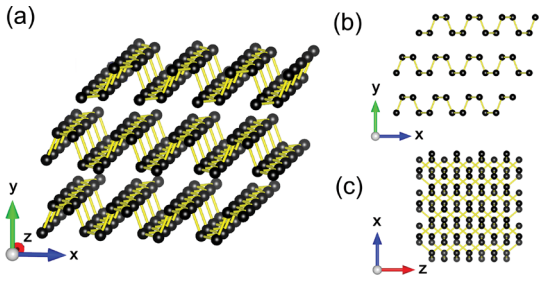

Figure 1. Crystalline structure of black phosphorus, represented in a (a) perspective view, (b) side view, and (c) top view for three stacked layers.

RESULTS AND DISCUSSION

Figure 1 illustrates the BP crystal structure from three different perspectives. We will adopt in this work the conventional definition of the crystallographic axes of BP, where the *y* axis is perpendicular to the layer plane, the *x* axis is along the armchair direction, and the *z* axis is along the zigzag direction.[19] The identification of the *x* and *z* axes of our sample, shown in Figure 2a, was done by comparison of the substrate's Raman band as measured directly and through BP as a function of θ and considering BP's linear dichroism as reported by Asahina *et al.*[27]

As explained in the Methods section, all experiments were performed in a backscattering geometry. The incident light was polarized always along the horizontal direction, as shown in Figure 2a, and an analyzer, placed before the entrance of the spectrometer, allowed for the analysis of the scattered light polarized parallel and perpendicular to the incident light polarization (parallel and cross-polarization configurations,

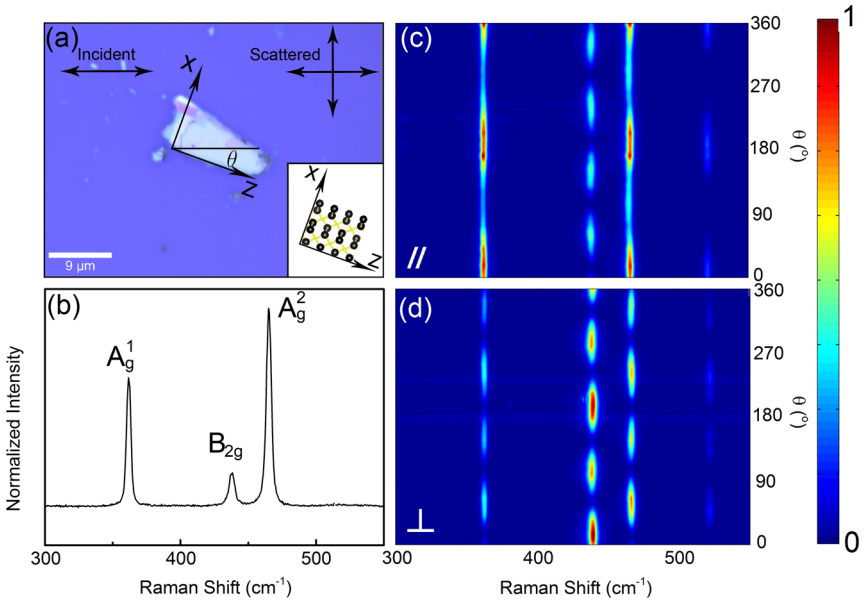

Figure 2. (a) Optical microscope image of the measured flake, showing the crystallographic axes, the directions of the incident and analyzed scattered light, and indicating the angle θ between the incident light and the *z* axis. (b) Raman spectrum for an arbitrary configuration showing the A_g^1, B_{2g}, and A_g^2 modes. Angular dependence of the Raman intensity spectra measured in the (c) parallel and (d) cross-polarization configurations.

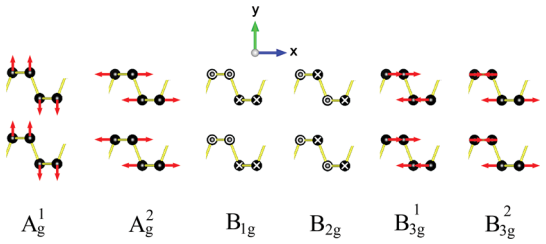

Figure 3. Atomic displacements of the Raman-active modes in BP.

TABLE 1. Raman Tensor Forms for All Active Modes in BP

mode	A_g	B_{1g}	B_{2g}	B_{3g}
tensor	$\begin{pmatrix} a & 0 & 0 \\ 0 & b & 0 \\ 0 & 0 & c \end{pmatrix}$	$\begin{pmatrix} 0 & d & 0 \\ d & 0 & 0 \\ 0 & 0 & 0 \end{pmatrix}$	$\begin{pmatrix} 0 & 0 & f \\ 0 & 0 & 0 \\ f & 0 & 0 \end{pmatrix}$	$\begin{pmatrix} 0 & 0 & 0 \\ 0 & 0 & g \\ 0 & g & 0 \end{pmatrix}$

respectively). The angular dependence of Raman response was obtained by rotating the sample in the *xz* plane, but the system of Cartesian coordinates adopted here remained parallel to the crystallographic axes.

According to the choice of crystallographic axes, the Raman-active modes of BP[22] are given by

$$2A_g + B_{1g} + B_{2g} + 2B_{3g} \quad (1)$$

The atomic displacements for the Raman modes in BP are schematically shown in Figure 3, and the Raman tensors for these modes are shown in Table 1. Since we have used a backscattering geometry and the laser beam propagates along the *y* direction, we can only analyze the polarized light in the *xz* plane. From the Raman tensor elements in Table 1, the spectra in this configuration will only show the A_g and B_{2g} modes because the B_{1g} and B_{3g} modes only have *xy* and *yz* non-null components, respectively.

Figure 2b shows a typical Raman spectrum of BP in the 300−550 cm^{-1} range. The three peaks at 360, 436, and 463 cm^{-1} are associated, respectively, with the A_g^1, B_{2g}, and A_g^2 modes, and these values are in good agreement with previous Raman results.[20] Figure 2c,d shows the angular dependence of the Raman spectra in the parallel and cross-polarization configurations, respectively. The low-intensity peak at 525 cm^{-1} is a Raman mode of the substrate. The intensities of the peaks are represented by the color scale shown in the right-hand side of these figures. The intensities of all spectra in each graph have been normalized by a single constant, so that the most intense peak has its intensity equal to 1. As we will discuss below, the absolute values of the obtained Raman tensor components for each laser line are solely dependent on this choice of normalization.

For a quantitative analysis of the angular dependence of the Raman intensities, let us first introduce the unitary vectors $\hat{\mathbf{e}}_i$ and $\hat{\mathbf{e}}_s$ that give the polarization of the incident and scattered light with respect to the crystallographic axes, as shown in Figure 2a. For the incident beam, $\hat{\mathbf{e}}_i = (\sin\theta \quad 0 \quad \cos\theta)$, while for scattered light, $\hat{\mathbf{e}}_s = (\sin\theta \quad 0 \quad \cos\theta)$ and $\hat{\mathbf{e}}_s = (\cos\theta \quad 0 \quad -\sin\theta)$ for the parallel and cross-polarization configurations, respectively. The Raman cross section, *S*, that gives the scattering intensity, is written as[28]

$$S_k \propto |\hat{\mathbf{e}}_i \cdot \overleftrightarrow{R^k} \cdot \hat{\mathbf{e}}_s|^2 \quad (2)$$

where $\overleftrightarrow{R^k}$ is the Raman tensor for the different symmetry modes given in Table 1, which are denoted by the index *k*.

We now analyze the data shown in Figure 2c,d using the conventional approach, in which the elements of the Raman tensor assume real values only. Substituting in eq 2 the unitary vectors $\hat{\mathbf{e}}_i$ and $\hat{\mathbf{e}}_s$ defined above and the Raman tensors shown in Table 1, we obtain the expressions for the angular dependencies of the A_g and B_{2g} intensities for both polarization configurations:

$$S_{A_g}^{\parallel} = (a\sin^2\theta + c\cos^2\theta)^2 \quad (3)$$

$$S_{A_g}^{\perp} = [(a - c)\cos\theta\sin\theta]^2 \quad (4)$$

$$S_{B_{2g}}^{\parallel} = (2f\cos\theta\sin\theta)^2 \quad (5)$$

$$S_{B_{2g}}^{\perp} = [f\cos(2\theta)]^2 \quad (6)$$

Figure 4 shows the Raman intensities as functions of the angle, θ, for the A_g^1, B_{2g}, and A_g^2 modes in the parallel and cross-polarization configurations, obtained with the 532 and 633 nm laser lines. The dots correspond to the experimental data, and the solid curves represent the best fits using eqs 3−6. Notice that the angular dependencies of the B_{2g} mode, in both polarization configurations and using the two different laser lines (Figure 4c,d,i,j), are nicely fitted by eqs 5 and 6, and from these fits, we can obtain the value of the Raman tensor element *f*. The angular dependencies of the A_g^1 mode obtained with the 532 nm laser line are also well fitted by eqs 3 and 4 (Figure 4a,b). However, as shown in Figure 4g,h, we cannot fit simultaneously the angular dependencies in the parallel and cross-polarization configurations for the A_g^1 mode and for the 633 nm laser line. Also, Figure 4e,f,k,l shows that the angular dependence of the A_g^2 is never well-fitted by eqs 3 and 4. Particularly for the parallel polarization configuration, the experimental data exhibit a secondary maximum at $\theta = 90°$ and $\theta = 270°$, which is never reproduced by the fitting curves. We therefore conclude that the conventional Raman approach, which considers the Raman tensor elements to be real, can nicely describe the angular dependence for the B_{2g} mode but clearly fails to explain the behavior of the totally symmetric A_g

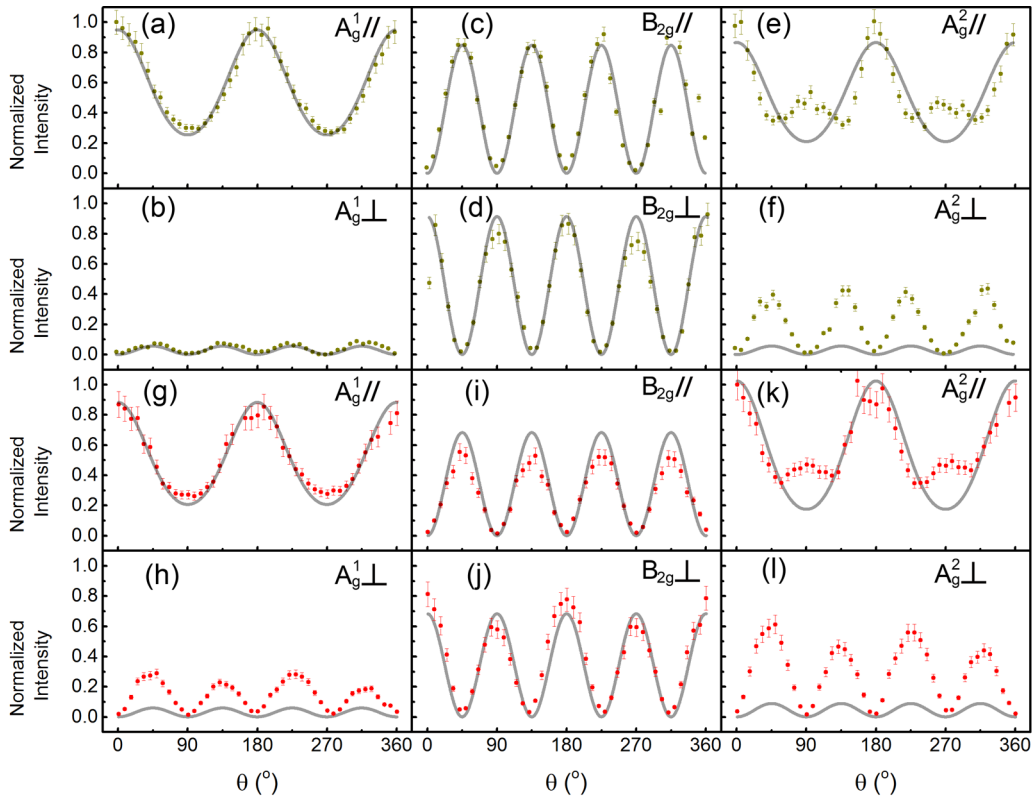

Figure 4. Angular dependence of the Raman intensities measured using the 532 nm laser line (a−f) and the 633 nm laser line (g−l). The polarization configurations (parallel or cross) and the different Raman modes are indicated in each panel. Dots are experimental data, and solid curves correspond to the best fits to the data using eqs 3−6 for each configuration and mode symmetry.

modes, in particular for the in-plane A_g^2 mode. As we will show below, this result is related to the linear dichroism of BP.[29]

In order to explain our results, we need to consider the impact of light absorption on the Raman tensor elements. In absorptive materials, each component ϵ_{ij} of the dielectric function tensor has real and imaginary parts and can be written as $\epsilon_{ij} = \epsilon_{ij}' + i\epsilon_{ij}''$. The element R_{ij}^k of the Raman tensor is given by the derivative of the dielectric function element ϵ_{ij} with respect to the normal coordinate q^k:[28,30]

$$R_{ij}^k = \frac{\partial \epsilon_{ij}}{\partial q^k} = \frac{\partial \epsilon_{ij}'}{\partial q^k} + i\frac{\partial \epsilon_{ij}''}{\partial q^k} \tag{7}$$

As a consequence, when there is absorption of light, the Raman tensor elements also present complex values, with real and imaginary parts. The Raman tensor elements relevant to this work (a, c, and f as defined in Table 1) can thus be written as

$$a = |a|e^{i\phi_a},\ c = |c|e^{i\phi_c},\ f = |f|e^{i\phi_f} \tag{8}$$

where the phases of the Raman tensor elements are given by

$$\phi_a = \text{arctg}\left[\frac{\frac{\partial \epsilon_{xx}''}{\partial q^{A_g}}}{\frac{\partial \epsilon_{xx}'}{\partial q^{A_g}}}\right],\ \phi_c = \text{arctg}\left[\frac{\frac{\partial \epsilon_{zz}''}{\partial q^{A_g}}}{\frac{\partial \epsilon_{zz}'}{\partial q^{A_g}}}\right],\ \phi_f = \text{arctg}\left[\frac{\frac{\partial \epsilon_{xz}''}{\partial q^{B_{2g}}}}{\frac{\partial \epsilon_{xz}'}{\partial q^{B_{2g}}}}\right] \tag{9}$$

Substituting in eq 2 the unitary vectors $\hat{\mathbf{e}}_i$ and $\hat{\mathbf{e}}_s$ and the complex values of the Raman tensor elements defined in eq 8, the angular dependencies for the A_g and B_{2g} mode intensities, in the parallel and cross-polarization configurations, are now given by

$$S_{A_g}^{\parallel} = (|a|\sin^2\theta + |c|\cos\phi_{ca}\cos^2\theta)^2 + |c|^2\sin^2\phi_{ca}\cos^4\theta \tag{10}$$

$$S_{A_g}^{\perp} = [(|a| - |c|\cos\phi_{ca})^2 + |c|^2\sin^2\phi_{ca}]\sin^2\theta\cos^2\theta \tag{11}$$

$$S_{B_{2g}}^{\parallel} = (2|f|\sin\theta\cos\theta)^2 \tag{12}$$

$$S_{B_{2g}}^{\perp} = [|f|\cos(2\theta)]^2 \tag{13}$$

Note that the expressions for the B_{2g} mode given by eqs 12 and 13 are identical to those obtained considering only real values for the Raman tensor elements (eqs 5 and 6). This is due to the fact that the phase ϕ_f is canceled out when we take the square modulus of the Raman efficiency expressions. However, this phase cancellation does not occur for the totally symmetric A_g modes, and we have now, in eqs 10 and 11, a term ϕ_{ca}, which is the phase difference $\phi_c - \phi_a$.

Figure 5 shows the experimental angular dependencies for the two A_g modes, together with the best fits provided by eqs 10 and 11. Figure 5a,b shows the

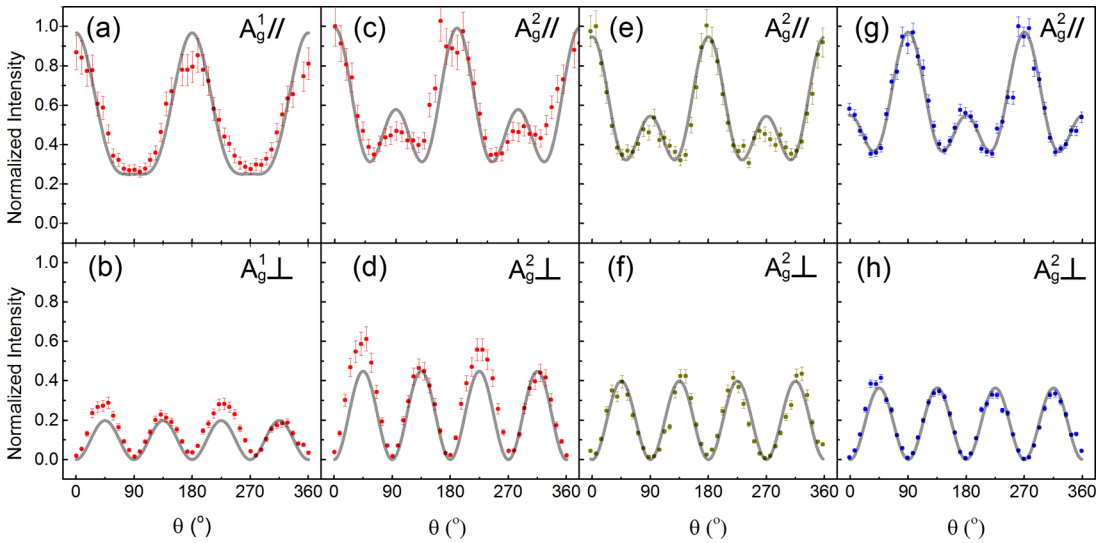

Figure 5. Angular dependence of the Raman intensities measured with the (a−d) 633 nm, (e,f) 532 nm, and (g,h) 488 nm laser lines. The polarization configurations (parallel or cross) and the different Raman modes are indicated in each panel. Dots are experimental data, and solid curves correspond to the best fits to the data using eqs 10 and 11 for each configuration and Raman mode.

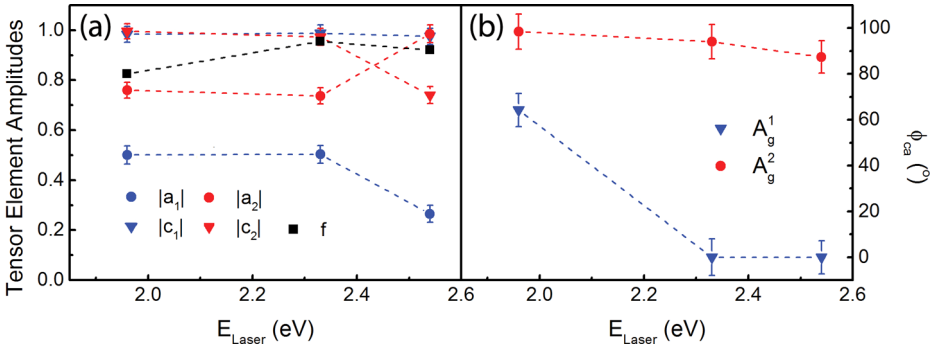

Figure 6. (a) Laser energy dependence of the absolute values of Raman tensor elements (|*a*|, |*c*|, or *f*). (b) Laser energy dependence of the phase diference $\phi_{ca} = \phi_c - \phi_a$ for the A_g^1 and A_g^2 modes.

angular dependence of the A_g^1 mode in the parallel and cross-polarization configurations obtained with the red laser line (633 nm). Figure 5c−h shows the angular dependencies of the A_g^2 mode in both parallel and cross-polarization configurations, obtained with the three laser lines (633, 532, and 488 nm). Notice that all angular dependencies are nicely fitted by introducing the phase difference ϕ_{ca}.[31]

Figure 6a shows the absolute values of the Raman tensor elements for the A_g^1, B_{2g}, and A_g^2 modes as functions of the laser energy. Those values are dependent solely on our choice of normalization of the peak intensities, where we attributed the unity value for the most intense peak for each laser line. We can observe in Figure 6a that the absolute values of the Raman tensor elements exhibit a laser energy dependence, which is, in fact, an expected result since the modulus of the Raman tensor elements depends on both the real and imaginary parts of the dielectric function, which are dispersive near electronic resonances. For the A_g^1 mode, the |*c*| parameter is always larger than the |*a*| parameter, showing that the component *zz* of the dielectric constant (zigzag direction) is more modulated by this specific phonon mode than the *xx* component. For the A_g^2 mode, |*c*| is larger than |*a*| for the red (633 nm) and green (532 nm) laser lines, but there is an inversion at higher energies, and |*c*| becomes smaller than |*a*| using the blue laser line (488 nm).

Figure 6b shows the laser energy dependence of the phase differences ϕ_{ca} for the A_g^1 and A_g^2 modes. First notice that ϕ_{ca} is larger for the A_g^2 mode than for the A_g^1 mode. In fact, this phase difference is practically zero for the A_g^1 mode with the 532 and 488 nm lines and about 64° when using the 633 nm line. On the other hand, ϕ_{ca} is quite large for the A_g^2 mode (around 90°), and this value slightly decreases with increasing laser energy.

Our results above show that the angular dependence of polarized Raman spectra of BP is rather unusual and can only be explained by considering complex values for the Raman tensor elements. These complex values are related to the fact that the material

absorbs the laser light. However, the phase of the complex values appears only in Raman spectra for the totally symmetric phonons and only for crystals with orthorhombic, monoclinic, or triclinic symmetries. For higher symmetry crystals, the phase of the totally symmetric modes disappears when we take the square modulus in eq 2, and therefore, they exhibit the usual angular dependence.

The complex values of the Raman tensor elements can be traced back to the electron−photon and electron−phonon interactions. The Raman scattering process described so far in this paper is based on the so-called semiclassical model. In this approach, the electronic polarizability depends only on the two electron−radiation processes (absorption of the incident photon and emission of the scattered photon). In this case, Raman scattering comes from the first-order term in the Taylor expansion of the polarizability with respect to the vibrational normal coordinates. The electron−phonon coupling is only explicitly taken into account in a full quantum description of Raman scattering, which corresponds to a third-order process involving two electron−radiation interactions and one electron−phonon interaction. A more in-depth discussion about the semiclassical and full quantum descriptions is presented in the Supporting Information.

Figure 6 shows that the relative phases ϕ_{ca} of the Raman tensor elements are different for the two totally symmetric modes (A_g^1 and A_g^2). This difference can only be due to the electron−phonon interaction because the electron−radiation matrix elements are the same for both totally symmetric modes. As also shown in the Supporting Information, the electron−phonon and electron−radiation matrix elements can also have complex values for BP, which are related to the amplitudes and phases of the Raman tensor components.

CONCLUSIONS

In this work, we presented an extensive polarized Raman characterization of black phosphorus using three different laser lines. The angular dependence of the polarized Raman spectra for the A_g^1, A_g^2, and B_{2g} modes in both parallel and cross-polarization configurations was measured, and an unusual behavior for the angular dependence of the totally symmetric mode intensities was observed. Our analysis, which accounts for the linear dichroism of black phosphorus, led us to conclude that the Raman tensors exhibit complex elements. This approach allowed us to measure the phase differences between Raman tensor elements for each mode and for each laser line, and it was observed that the phase differences are much larger for the in-plane totally symmetric A_g^2 than for the out-of-plane A_g^1 mode. The unusual form of the Raman tensor is interpreted as the result of the particular band structure, electron−radiation interaction, and electron−phonon coupling in this material, the latter of which is still poorly understood but of great importance for the understanding of the electronic phases of BP, especially superconductivity.

METHODS

Since BP is well-known to be susceptible to oxygen,[32−34] the samples were prepared by mechanical exfoliation in a pure nitrogen environment, being transferred onto 300 nm silicon dioxide on silicon wafers. Polarized Raman experiments were performed in individual BP single-crystal flakes with thicknesses of hundreds of nanometers (the results shown are for a 360 nm thick flake) using a confocal microscope spectrometer (WITec Alpha 300R) with a 100× objective lens and using 488 nm (2.54 eV), 532 nm (2.33 eV), and 633 nm (1.96 eV) laser lines. The laser power and spectrometer integration time were 2.0 mW and 0.5 s, respectively, for all measurements. We used a backscattering geometry, and the sample was continuously purged with nitrogen during the experiments.

The incident laser beam is polarized, and an analyzer was placed just before the spectrometer entrance, allowing the investigation of the scattered light polarization along directions parallel and perpendicular to the incident light polarization. Throughout the paper, these two polarization configurations are called, respectively, the parallel and cross-polarization configurations and are represented in Figure 2a, where the angle θ between the incident light polarization and the crystalline z direction is also defined. The sample was rotated 360° about the microscope optical axis in 44 steps, allowing the measurement of the angular dependence of the Raman intensities in both polarization configurations. In every step, the flake position was adjusted in order to ensure that the same point was always probed, and the microscope focus was optimized.

Conflict of Interest: The authors declare no competing financial interest.

Acknowledgment. This work is supported by Fapesp (SPEC project 2012/50259-8) and partially supported by the Brazilian Nanocarbon Institute of Science and Technology (INCT/Nanocarbono) and CNPq. H.B.R. and J.D.Z. acknowledge CNPq scholarships. J.D.Z. acknowledges CODI (MDC 11-1-06) Universidad de Antioquia. A.H.C.N. acknowledges the National Research Foundation, Prime Minister's Office, Singapore, under its Medium Sized Centre Programme and CRP award "Novel 2D materials with tailored properties: beyond graphene" (R-144-000-295-281).

Supporting Information Available: An in-depth discussion about the semiclassical *versus* full quantum model for Raman scattering, as well as the relation between the complex nature of the measured Raman responses with black phosphorus's band structure and electron−radiation and electron−phonon interactions. This material is available free of charge *via* the Internet at http://pubs.acs.org.

REFERENCES AND NOTES

1. Koenig, S. P.; Doganov, R. A.; Schmidt, H.; Castro Neto, A. H.; Özyilmaz, B. Electric Field Effect in Ultrathin Black Phosphorus. *Appl. Phys. Lett.* **2014**, *104*, 103106.
2. Li, L.; Yu, Y.; Ye, G. J.; Ge, Q.; Ou, X.; Wu, H.; Feng, D.; Chen, X. H.; Zhang, Y. Black Phosphorus Field-Effect Transistors. *Nat. Nanotechnol.* **2014**, *9*, 372–377.

3. Lu, W.; Nan, H.; Hong, J.; Chen, Y.; Zhu, C.; Liang, Z.; Ma, X.; Ni, Z.; Jin, C.; Zhang, Z. Plasma-Assisted Fabrication of Monolayer Phosphorene and Its Raman Characterization. *Nano Res.* **2014**, 1–7.
4. Qiao, J.; Kong, X.; Hu, Z.-X.; Yang, F.; Ji, W. High-Mobility Transport Anisotropy and Linear Dichroism in Few-Layer Black Phosphorus. *Nat. Commun.* **2014**, *5*, 4475.
5. Liu, H.; Neal, A. T.; Zhu, Z.; Luo, Z.; Xu, X.; Tománek, D.; Ye, P. D. Phosphorene: An Unexplored 2D Semiconductor with a High Hole Mobility. *ACS Nano* **2014**, *8*, 4033–4041.
6. Buscema, M.; Groenendijk, D. J.; Blanter, S. I.; Steele, G. A.; van der Zant, H. S.; Castellanos-Gomez, A. Fast and Broadband Photoresponse of Few-Layer Black Phosphorus Field-Effect Transistors. *Nano Lett.* **2014**, *14*, 3347–3352.
7. Castellanos-Gomez, A.; Vicarelli, L.; Prada, E.; Island, J. O.; Narasimha-Acharya, K.; Blanter, S. I.; Groenendijk, D. J.; Buscema, M.; Steele, G. A.; Alvarez, J.; et al. Isolation and Characterization of Few-Layer Black Phosphorus. *arXiv:1403.0499* **2014**, 10.1088/2053-1583/1/2/025001.
8. Strach, T.; Brunen, J.; Lederle, B.; Zegenhagen, J.; Cardona, M. Determination of the Phase Difference between the Raman Tensor Elements of the A_g^1-like Phonons in $SmBa_2Cu_3O_{7-\delta}$. *Phys. Rev. B* **1998**, *57*, 1292.
9. Rodin, A.; Carvalho, A.; Castro Neto, A. H. Strain-Induced Gap Modification in Black Phosphorus. *Phys. Rev. Lett.* **2014**, *112*, 176801.
10. Kawamura, H.; Shirotani, I.; Tachikawa, K. Anomalous Superconductivity and Pressure Induced Phase Transitions in Black Phosphorus. *Solid State Commun.* **1985**, *54*, 775–778.
11. Rajagopalan, M.; Alouani, M.; Christensen, N. Calculation of Band Structure and Superconductivity in the Simple Cubic Phase of Phosphorus. *J. Low Temp. Phys.* **1989**, *75*, 1–13.
12. Brown, A.; Rundqvist, S. Refinement of the Crystal Structure of Black Phosphorus. *Acta Crystallogr. Commun.* **1965**, *19*, 684–685.
13. Morita, A. Semiconducting Black Phosphorus. *Appl. Phys. A: Mater. Sci. Process.* **1986**, *39*, 227–242.
14. Warschauer, D. Electrical and Optical Properties of Crystalline Black Phosphorus. *J. Appl. Phys.* **1963**, *34*, 1853–1860.
15. Narita, S.; Akahama, Y.; Tsukiyama, Y.; Muro, K.; Mori, S.; Endo, S.; Taniguchi, M.; Seki, M.; Suga, S.; Mikuni, A.; et al. Electrical and Optical Properties of Black Phosphorus Single Crystals. *Physica B + C* **1983**, *117*, 422–424.
16. Keyes, R. W. The Electrical Properties of Black Phosphorus. *Phys. Rev.* **1953**, *92*, 580–584.
17. Cartz, L.; Srinivasa, S.; Riedner, R.; Jorgensen, J.; Worlton, T. Effect of Pressure on Bonding in Black Phosphorus. *J. Chem. Phys.* **1979**, *71*, 1718–1721.
18. Vanderborgh, C.; Schiferl, D. Raman Studies of Black Phosphorus from 0.25 to 7.7 GPa at 15 K. *Phys. Rev. B* **1989**, *40*, 9595.
19. Sugai, S.; Ueda, T.; Murase, K. Pressure Dependence of the Lattice Vibration in the Orthorhombic and Rhombohedral Structures of Black Phosphorus. *J. Phys. Soc. Jpn.* **1981**, *50*, 3356–3361.
20. Kaneta, C.; Katayama-Yoshida, H.; Morita, A. Lattice Dynamics of Black Phosphorus. *Solid State Commun.* **1982**, *44*, 613–617.
21. Kaneta, C.; Katayama-Yoshida, H.; Morita, A. Lattice Dynamics of Black Phosphorus. I. Valence Force Field Model. *J. Phys. Soc. Jpn.* **1986**, *55*, 1213–1223.
22. Sugai, S.; Shirotani, I. Raman and Infrared Reflection Spectroscopy in Black Phosphorus. *Solid State Commun.* **1985**, *53*, 753–755.
23. Akahama, Y.; Endo, S. Transport Study on Pressure-Induced Band Overlapped Metallization of Layered Semiconductor Black Phosphorus. *Solid State Commun.* **1997**, *104*, 307–310.
24. Fei, R.; Yang, L. Lattice Vibrational Modes and Raman Scattering Spectra of Strained Phosphorene. *Appl. Phys. Lett.* **2014**, *105*, 083120.
25. Zhang, S.; Yang, J.; Xu, R.; Wang, F.; Li, W.; Ghufran, M.; Zhang, Y.-W.; Yu, Z.; Zhang, G.; Qin, Q.; et al. Extraordinary Photoluminescence and Strong Temperature/Angle-Dependent Raman Responses in Few-Layer Phosphorene. *ACS Nano* **2014**, *8*, 9590–9596.
26. Wu, J.; Mao, N.; Xie, L.; Xu, H.; Zhang, J. Identifying the Crystalline Orientation of Black Phosphorus Using Angle-Resolved Polarized Raman Spectroscopy. *Angew. Chem.* **2015**, *127*, 2396–2399.
27. Asahina, H.; Morita, A. Band Structure and Optical Properties of Black Phosphorus. *J. Phys. C: Solid State Phys.* **1984**, *17*, 1839.
28. Loudon, R. The Raman Effect in Crystals. *Adv. Phys.* **1964**, *13*, 423–482.
29. Low, T.; Rodin, A. S.; Carvalho, A.; Jiang, Y.; Wang, H.; Xia, F.; Castro Neto, A. H. Tunable Optical Properties of Multilayer Black Phosphorus Thin Films. *Phys. Rev. B* **2014**, *90*, 075434.
30. Cardona, M. *Light Scattering in Solids II*; Springer: Berlin, 1982.
31. We highlight that our results, both experimental and theoretical, allow one to conclude that aligning the incident polarization to the zigzag crystallographic direction ($\theta = 0°$) leads to the observation of the main peak of the A_g^2 mode in the parallel configuration, while a secondary peak is observed when the incident polarization is parallel to the armchair direction ($\theta = 90°$). This conclusion is the exact opposite to that presented in ref 26. We believe this discrepancy can be explained by an incorrection in the angular dependence of the hole conductance used in ref 26. A detailed discussion on this subject will be published elsewhere.
32. Ziletti, A.; Carvalho, A.; Trevisanutto, P. E.; Campbell, D. K.; Coker, D. F.; Castro Neto, A. H. Phosphorene Oxides: Bandgap Engineering of Phosphorene by Oxidation. *Phys. Rev. B* **2015**, *91*, 085407.
33. Island, J. O.; Steele, G. A.; van der Zant, H. S. J.; Castellanos-Gomez, A. Environmental Instability of Few-Layer Black Phosphorus. *2D Mater.* **2015**, *2*, 011002.
34. Favron, A.; Gaufrès, F.; Fossard, E.; Lévesque, P.; Phaneuf-L'Heureux, A.-L.; Tang, N. Y.-W.; Loiseau, A.; Leonelli, R.; Francoeur, S.; Martel, R. Exfoliating Pristine Black Phosphorus down to the Monolayer: Photo-oxidation and Electronic Confinement Effects. *arXiv:1408.0345* **2014**.